

Modeling Noisy Quantum Circuits Using Experimental Characterization

Megan N. Lilly^{1,2} and Travis S. Humble^{1,2}

¹Quantum Computing Institute, Oak Ridge National Laboratory, Oak Ridge, Tennessee, USA

²Bredesen Center for Interdisciplinary Research and Graduate Education, University of Tennessee, Knoxville, USA

23 DEC 2019

Noisy intermediate-scale quantum (NISQ) devices offer unique platforms to test and evaluate the behavior of non-fault-tolerant quantum computing. However, validating programs on NISQ devices is difficult due to fluctuations in the underlying noise sources and other non-reproducible behaviors that generate computational errors. Efficient and effective methods for modeling NISQ behaviors are necessary to debug these devices and develop programming techniques that mitigate against errors. We present a test-driven approach to characterizing NISQ programs that manages the complexity of noisy circuit modeling by decomposing an application-specific circuit into a series of bootstrapped experiments. By characterizing individual subcircuits, we generate a composite model for the original noisy quantum circuit as well as other related programs. We demonstrate this approach using a family of superconducting transmon devices running applications of GHZ-state preparation and the Bernstein-Vazirani algorithm. We measure the model accuracy using the total variation distance between predicted and experimental results, and we find that the composite model works well across multiple circuit instances. In addition, these characterizations are computationally efficient and offer a trade-off in model complexity that can be tailored to the desired predictive accuracy.

1 Introduction

Quantum computing is a promising approach to accelerate computational workflows by solving problems with greater accuracy or using fewer resources as compared to conventional methods [1, 2, 3, 4]. Testing and evaluation of early applications on experimental quantum processing units (QPUs) is now possible using prototypes based on superconducting transmons

Megan N. Lilly: lillymn@ornl.gov, <https://orcid.org/0000-0002-5747-9695>

Travis S. Humble: humblets@ornl.gov, <https://orcid.org/0000-0002-9449-0498>

[5, 6, 7, 8] and trapped ions [9, 10, 11, 12] among other technologies. Although these QPUs lack the fault-tolerant operations required for known computational speed ups, they offer the opportunity to understand the behaviors of noisy quantum computing [13].

Noisy, intermediate-scale quantum (NISQ) devices have enabled a wide range of early application demonstrations [14, 15, 16, 17, 18, 6], but validating program performance in the presence of non-reproducible device behaviors remains a fundamental challenge. NISQ devices are characterized by noisy and erroneous operations, where gate characterizations often change in time and with the nature of the program being implemented [19, 20]. The experimental characterization of individual gates has relied on high-fidelity physics models for the underlying devices with common methods including quantum state tomography (QST) [21], quantum process tomography (QPT) [22, 23], gate-set tomography (GST) [24], and randomized benchmarking (RB) [25, 26, 27]. Although these physics-driven characterizations are generally resource intensive, they offer valuable insights into the underlying noise and errors that can inform the design of new devices and control pulses.

As NISQ applications evolve toward deeper and wider quantum circuits, characterization methods must also extend to these larger scales. There is also a growing need for characterization techniques that can be executed swiftly and repeatedly to provide context-specific characterization data. Resource-intensive, physics-driven gate characterization techniques are not a scalable solution to characterizing devices and applications which are rapidly increasing in size and generally do not allow for a high level of dynamic tuning. Quantum circuit characterization methods may provide effective models of device behaviors that are efficient to generate and easy to interpret by a supporting programming environment, e.g., a compiler [28, 29, 30]. In particular, the validation of application behavior will require debugging methods and programming techniques that support mitigating computational errors in quantum circuits [31, 32]. Effective models of noisy gates and circuits have already informed robust programming methods that lead to increased application performance [33, 34, 35], but a

general method for composing noisy quantum circuit models is still needed.

In this contribution, we introduce methods for generating effective models for noisy quantum circuits in NISQ devices derived from experimental characterization. Our approach is based on modeling application-specific circuits using a suite of characterization tests that build a representative set of noisy subcircuit models. We compose noisy subcircuit models to generate noise models for more complicated circuits at larger scales, and we test the fidelity of the resulting model against experimental data. We show how to iteratively adjust the composite model selected for a noisy application circuit by comparing performance of the predicted behavior against application observations using the total variation distance (TVD) [33]. The iterative and flexible nature of this modeling approach is demonstrated using applications based on GHZ-state preparation and the Bernstein-Vazirani algorithm for search. We develop model composition for the fixed-frequency superconducting transmon devices available from IBM, though we propose these techniques may extend to other NISQ devices as well.

This characterization method is a coarse-grained yet fast approach to characterization which scales linearly with the number of elements in the device, e.g. qubits and couplings. Furthermore, it allows for dynamic tuning of characterization data to every execution of a particular application and can be tailored to yield desired information, e.g. development of a noise model using depolarizing parameters or performance of an entangling gate creating an equal superposition. The tradeoff compared to physics-driven characterization techniques is less total information received, which in some cases may result in a lower accuracy in the final effective description of the device.

We present the steps in the modeling methodology in Sec. 2 followed by a series of examples using the case of n -qubit GHZ states in Sec. 3. In Sec. 4, we present results from experimental characterization for the GHZ state on NISQ QPUs and discuss the role of model selection for characterization accuracy. In Sec. 5, we apply these models to the case of the n -bit Bernstein-Vazirani algorithm, while we offer final conclusion in Sec. 7.

2 Model Selection Methodology

We begin by providing an overview of the modeling methodology before providing specific examples of its implementation. Consider the input for noisy circuit modeling to be an idealized quantum circuit C that is expressed in the available instruction set architecture (ISA) for a given QPU [2]. While the gates defined by the ISA may not be directly implemented within the QPU, the representation used for the ideal circuit will define the operators available for gate characterization. The input circuit is decomposed into a set

$S(C) = \{S_i\}$ of idealized subcircuits S_i that each include some of the gates and register elements defined by the original input. This decomposition will define noise characterization and every gate and register element within the input circuit must be included in at least one subcircuit for complete characterization. These subcircuits are generally not disjoint. Under this constraint, the number of subcircuits $|S|$ scales with the area of C and the decomposition method. The size of each subcircuit remains fixed. For example, a circuit consisting of only one- and two-qubit gates may be decomposed into a set of two-qubit subcircuits, while the optimal decomposition for characterization will depend on the potentially unknown device noise.

A set of tests is generated to characterize the noise of each subcircuit in S . Each test circuit specifies an input state and the idealized outcome for the subcircuit instance. The simplest realization is to generate input states that are separable in the computational basis, i.e., $|b_1, b_2, \dots, b_n\rangle$ for binary values b_i , but other state preparations may be useful as well. We select state preparations to be informative yet limited in order to increase efficiency and improve scalability. We denote the resulting set of test circuits as $T = \{T_i\}$, which is at least as large as S and generally larger. For example, given only two-qubit subcircuits tested in the computational basis, then $|T| = 4|S|$.

The implementation and execution of test circuits on a QPU generates a corresponding set of measurement observations. Each test circuit is executed multiple times to gather statistics from the distribution of results R_i that characterize subcircuit T_i . The i -th characterization is denoted as $H_i = (T_i, R_i)$ and the set of all characterizations is given as H . The number of characterizations is fixed by the number of test circuits $|T|$, while the number of measurement observations acquired for each test circuit is set by the sampling parameter N_s . Assuming the same sampling for all tests, then there are a total of $N_s|T|$ measurement observations, i.e., experiments, required for H .

The results of experimental characterization are used to formulate concise approximate models of the subcircuits' observed behaviors. We model each noisy subcircuit as the idealized subcircuit followed by a quantum channel that accounts for the noise [36]. Let the noisy subcircuit model $M_i = M(S_i, p_i)$ representing subcircuit S_i depend on model parameters p_i . We estimate the channel parameters using the characterization H_i , where the method of parameter estimation will vary with the selected model. Parameter estimation may be either direct or optimized methods. For example, least-square error estimates may be used to estimate parameters from noisy measurement observations by optimizing the residual model error.

We quantify the error in the resulting models using the total variation distance (TVD) [33], which is

defined as

$$d_{\text{TV}}(H_i, M_i) = \frac{1}{2} \sum_k \left| f_k(H_i) - f_k(M_i) \right| \quad (1)$$

where $f_k(H_i)$ is the frequency with which the k -th outcome of the test circuit T_i is observed and $f_k(M_i)$ is the corresponding frequency predicted by the noisy circuit model. In practice, each $f_k = C_k/N_s$, where C_k is the number of events observed for each measurement. The TVD vanishes as the predictions of the model become more accurate in reproducing the observed results and reaches a maximum of unity when the sets are completely disjoint.

After estimating the model parameters $p = \{p_i\}$ for all subcircuits, the corresponding noisy circuit model $M(C, p)$ for the input circuit C is composed. The method of composition of the noisy subcircuit models is paired with the decomposition method to ensure a consistent representation of the original input circuit. In the examples below, we consider modeling methods based on independent noisy subcircuit models that permit separable composition-decomposition methods and defer discussion of non-separable models, e.g., context-dependent noise, to Sec. 7.

Final selection of the noisy circuit model is then guided by the accuracy with which the composite model reproduces the performance of the circuit C on the QPU. For clarity, we define the actual executed circuit $A = (C, R_c)$ with R_c the recorded results, and we measure the accuracy of the noisy circuit model as $d_{\text{TV}}(A, M)$. The desired TVD sets an upper bound on the threshold for model accuracy. If this user-defined threshold is not satisfied, selection of the noisy subcircuit models is revisited. This iteration may include refinement of the noisy subcircuit models to improve the accuracy of each M_i or redefinition of the circuit composition-decomposition methods to manage the trade-offs in modeling complexity and accuracy. The former requires repeated post-processing analysis of the characterization H , whereas the latter requires additional characterization testing. In either case, model selection continues until the threshold has been met. Once the accuracy threshold has been satisfied, noisy circuit modeling is complete.

The noisy subcircuit models can then be tested for robustness in predicting the expected outcome from both the input circuit and other circuits executed on the characterized device. We again use TVD to measure the accuracy for selected models to characterize the behavior of other application circuits within the same QPU context.

3 Application to GHZ States

We next illustrate the methodology of Sec. 2 using the example of a GHZ-state preparation and measurement circuit. We generate noisy quantum circuit

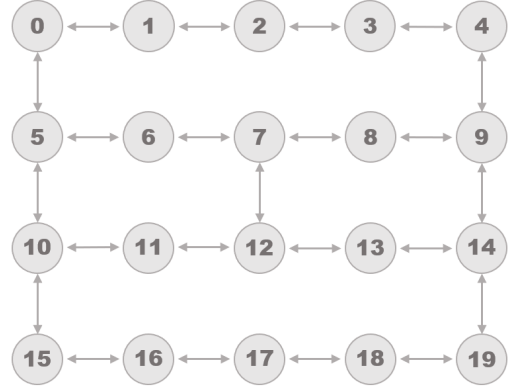


Figure 1: A graphical representation of the register connectivity in the *poughkeepsie* QPU at the time of data collection, in which each node corresponds to a register element and directional edges indicate the availability of a programmable two-qubit cross-resonance gate.

models for this application for various circuit sizes executed on the IBM *poughkeepsie* QPU, which has a register and layout as shown in Fig. 1. All data for characterization tests and applications is collected in a single job sent to *poughkeepsie*, a process which typically required under 30 minutes of execution time after queuing. As the *poughkeepsie* device is periodically calibrated, our experimental demonstrations ensure that all data is collected within one calibration window to preserve the QPU context. The software implementation of our examples below is available publicly [37].

We consider the example of preparing the n -qubit GHZ state

$$|\text{GHZ}(n)\rangle = \frac{1}{\sqrt{2}} (|0_1, 0_2, \dots, 0_n\rangle + |1_1, 1_2, \dots, 1_n\rangle) \quad (2)$$

where the subscript denotes the qubit and the schematic representation of the input circuit C is given in Fig. 2. The instruction set for this circuit is limited to the one-qubit Hadamard (H) and two-qubit controlled-NOT (CNOT) unitaries along with the initialization and readout gates acting on a quantum register of size n . We study this example for a range of register sizes from $n = 2$ to 20 by composing a noisy circuit model that represents GHZ-state preparation on a QPU based on superconducting transmon technology [38, 39]. This example demonstrates the unique features of superposition and entanglement using a circuit depth that is within the capabilities of the NISQ devices [40, 41].

We decompose this input circuit into a set of subcircuits S based on the four primary functions of the circuit, i.e., initialization and measurement, preparation of a single-qubit state, and preparation of a two-qubit entangled state. Spatial variability in the device noise motivates a decomposition based on each register element q_i . We extend these subcircuits to generate a corresponding set of test circuits T defined with respect to input state in the computational basis. The

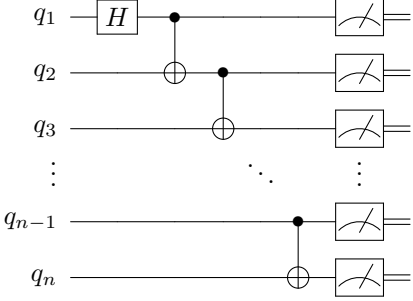


Figure 2: The schematic representation of the quantum circuit used for preparation of the n -qubit GHZ state defined by Eq. (2). The circuit layout satisfies the connectivity constraints of the IBM *poughkeepsie* QPU shown in Fig. 1. The circuit uses a total of $n - 1$ CNOT gates and n measurement gates.

expected outcomes of these particular test circuits are simple to calculate from the truth tables for each operator [42]. We examine the models using these test circuits.

3.1 Noisy Measurement Model

We begin by characterizing the initialization and measurement subcircuits, which are necessary for modeling noisy unitary gate behavior. The measurement process for each register element discriminates an analog signal to generate a classical bit [43], and errors in signal discrimination may lead to the wrong value. Characterization of measurement records the number and type of outcomes observed for each initial state. We characterize each register element with respect to both the 0 and 1 output states. The leading errors in the observed results occurs when the j -th register element maps an expected output value to its complement, i.e., $0 \rightarrow 1$ and $1 \rightarrow 0$.

We model measurement of the j -th element as a binary process subject to errors which act on the post-measurement classical bit string, and we consider two models for the measurement error process: symmetric readout noise (SRO) and asymmetric readout noise (ARO). The SRO model is defined by a single parameter p_{sro} that specifies the probability for a bit to flip, and we define a test circuit to characterize this process as measurement immediately after initialization to state $|0\rangle$. We directly estimate the value of p_{sro} from the number of errors when preparing this computational basis state as $p_{sro} = g(1)$, where $g(k)$ is the frequency of k errors recorded. This model implicitly delegates initialization errors to the readout error model. The SRO model is developed by subcircuits $S = \{S_{init.}\}$ and test circuits $T = \{T_{init.}(|0\rangle)\}$ where $|S| = |T| = 1$. The final SRO model is defined by $M_{SRO} = M(S_{init.}, p_{SRO})$.

By contrast, the ARO model uses two parameters: p_0 for the probability of error in readout of

$|0\rangle$ and p_1 as the probability of error in readout of $|1\rangle$. We may estimate p_0 using the same test circuit above, but we must extend the characterization to preparation and measurement of $|1\rangle$ to estimate p_1 . These additional test circuits will require inclusion of the single-qubit X gate, and we also add a test circuit for the XX operation of two successive X gates applied to a single qubit. The latter reproduces the initial state $|0\rangle$, enabling the error in readout of state $|1\rangle$ to be isolated from the error associated with the X gate. The ARO model is therefore defined by $M_{ARO} = M(S_{init.}, p_0, p_1)$ where $T = \{T_{init.}(|0\rangle), T_{init.}(|1\rangle), T_{XX}(|0\rangle)\}$.

We model the test circuits for the ARO process using an isotropic depolarizing channel parameterized by p_x to describe noise in the X gate,

$$\epsilon_{DP}(\rho) = (1 - p_x)I\rho I + \frac{p_x}{3}(X\rho X + Y\rho Y + Z\rho Z) \quad (3)$$

where I , X , Y , and Z are the Pauli operators. Characterization of the ARO model yields an over-determined system of equations relating the four experimentally observed frequencies $g^{(X)}(0)$, $g^{(X)}(1)$, $g^{(XX)}(0)$ and $g^{(XX)}(1)$ to the parameters p_0 , p_1 , and p_x . Of these parameters, only the latter two are unknown since p_0 is determined by the same method outlined above for p_{SRO} . Because the experimental observations directly relate to each other via $g^{(X)}(0) + g^{(X)}(1) = 1$ and $g^{(XX)}(0) + g^{(XX)}(1) = 1$, we select the following system of equations for each register element based on counts of $g^{(·)}(0)$.

$$g^{(X)}(0) = \frac{2p_x}{3}\left(1 - p_0\right) + p_1\left(1 - \frac{2p_x}{3}\right) \quad (4)$$

$$g^{(XX)}(0) = (1 - p_0) \left[\left(1 - \frac{2p_x}{3}\right)^2 + \left(\frac{2p_x}{3}\right)^2 \right] + p_1 \left[\frac{4p_x}{3} \left(1 - \frac{2p_x}{3}\right) \right] \quad (5)$$

This system of equations is solved using the SciPy function `fsolve`, which is based on Powell's hybrid method for minimization [44].

3.2 Noisy Subcircuit Models

Test circuits for characterizing noisy subcircuits generate results that include measurement noise. We use the noisy measurement model above to account for these behaviors when modeling the results from test circuits. For the SRO and ARO models discussed above, this directly estimates the probabilities expected to be observed for each register. We use this procedure when discussing the characterization below.

We first characterize the subcircuit representing the Hadamard operation. The test circuit for a single Hadamard is defined with respect to the expected values for input states drawn from the computational

basis, which yield a uniform superposition of binary results upon ideal measurement. We also use even-parity sequences of Hadamard gates as a second test to estimate noise in the subcircuit. These test circuits $T = \{T_H(|0\rangle), T_{HH}(|0\rangle), T_{4H}(|0\rangle), T_{6H}(|0\rangle), \dots, T_{nH}\}$ are used to characterize S_H to yield $M_H(S_H, p_H)$.

We define test circuits for the CNOT operations that mirror the subcircuits used in the target application. For GHZ-state preparation, these are based on characterization of Bell-state preparation. The test circuit specification shown in Fig. 3 produces the idealized result of a uniform distribution over perfectly correlated binary values. These test circuits are defined across all pairings of register elements as represented by Fig. 2. For convenience, we will denote the Bell-state preparation subcircuit as $U_{\text{BS}}^{(j,k)} = U_{(\text{CNOT})}^{(j,k)} H^{(j)} |0_j, 0_k\rangle$.

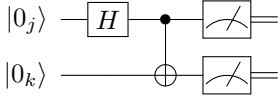


Figure 3: The test circuit for characterizing the CNOT operation acting on register elements q_j and q_k . This test prepares the two-qubit Bell state as an instance of $n = 2$ in Fig. 2.

The noisy test circuits for Bell-state preparation are modeled by a pair of identical, independent depolarizing channels. Each channel, together defined as $\epsilon_{DP}^{j,k} = \epsilon_{DP}^j \otimes \epsilon_{DP}^k$, is parameterized by p_{CNOT} , which represents the probability of a depolarizing error determined independently for each qubit in the two-qubit CNOT gate. We therefore use the test circuit $T = \{T_{\text{BS}}^{(j,k)}(|0_j, 0_k\rangle)\}$ generated by $S = \{S_{\text{CNOT}}\}$ for $S_{\text{CNOT}} = U_{\text{BS}}^{(j,k)}$ to compose model $M_{\text{CNOT}} = M(S_{\text{CNOT}}, p_{\text{CNOT}})$.

The frequency of observing bits a and b is given by

$$f_{j,k}(ab) = \text{Tr} \left[\Pi_{ab} \epsilon_{DP}^{j,k} \left(U_{\text{BS}}^{(j,k)} |0_j, 0_k\rangle \langle 0_j, 0_k| U_{\text{BS}}^{(j,k)\dagger} \right) \right] \quad (6)$$

where the operator Π_{ab} projects onto the state $|a, b\rangle$, and the resulting trace yields the probability of the ideal measurement. The frequencies expected from the noisy Bell state subcircuit on qubits j, k with ideal measurement is then given by

$$f_{j,k}(00) = f_{j,k}(11) = \frac{1}{2} - \frac{2}{3}p_{\text{CNOT}} + \frac{4}{9}p_{\text{CNOT}}^2 \quad (7)$$

$$f_{j,k}(01) = f_{j,k}(10) = \frac{2}{3}p_{\text{CNOT}} - \frac{4}{9}p_{\text{CNOT}}^2$$

Errors in readout transform these frequencies according to the noisy process, which may be either the SRO or ARO model. For example, the frequency following

readout $h_{j,k}(00)$ under the ARO channel is given by

$$\begin{aligned} h_{j,k}(00) = & (1 - p_0^j)(1 - p_0^k)f_{j,k}(00) \\ & + (1 - p_0^j)p_1^k f_{j,k}(01) \\ & + p_1^j(1 - p_0^k)f_{j,k}(10) \\ & + p_1^j p_1^k f_{j,k}(11) \end{aligned} \quad (8)$$

From the system of four equations generated by the readout frequencies $h_{j,k}(cd)$, we use the method of least squares to estimate p_{CNOT} . We minimize the sum of the squared residuals,

$$\sum_{cd} \left(h_{j,k}(cd) - g_{j,k}(cd) \right)^2 \quad (9)$$

where each residual is defined as the difference between the modeled frequency $h_{j,k}(cd)$ and the experimentally observed frequency $g_{j,k}(cd)$ for each state result cd . The value $g_{j,k}(cd)$ represents the counts of state cd on qubits j, k measured during a total number of experiments N_s . The value returned for p_{CNOT} is found using the SciPy `fsoolve` function and bounded between 0 and 1 [44].

4 Experimental Characterization

In this section, we report on the results of experimental characterization and noisy circuit modeling of GHZ-state preparation using a QPU based on superconducting transmon technology developed by IBM. The IBM *poughkeepsie* device has a register of 20 superconducting transmon elements that encode quantum information as a superposition of charge states [45]. Microwave pulses drive transitions between the possible charge configurations and induce single-qubit gates. Coupling between register elements uses a cross-resonance gate that drives a mutual transition between transmons and therefore only occurs between two spatially connected elements [38].

The layout of the 20-qubit register in *poughkeepsie* at the time of data collection is shown in Fig. 1. A common edge in the connectivity diagram specifies those register elements that may interact through the cross-resonance operation. Individual registers are measured through coupling to a readout resonator, which results in a state-dependent change in the resonator frequency. Amplification of the readout signal then enables discrimination of the state using a quantum non-demolition measurement [46, 5].

Circuits are sent to the backend where they are translated into the appropriate ISA. The ISA for *poughkeepsie* consists of the gates U_1 , U_2 , U_3 , CX , and ID [47]. The U_1 , U_2 , and U_3 gates are unitary rotation operators, of which U_1 is a “virtual” gate performed in software and U_2 and U_3 are performed in hardware. The identity gate ID is used as a placeholder to create a timestep since it does not alter a

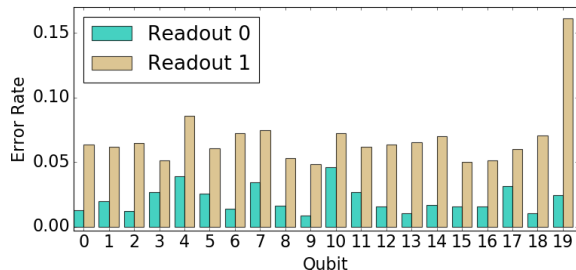


Figure 4: Error rates under the ARO channel for each qubit of *poughkeepsie*. The SRO channel is given by the error rates for state 0 shown here. Average p_0 value is 0.0212 (standard deviation of 0.0101 across all qubits) and average p_1 value is 0.0681 (standard deviation of 0.0233).

quantum state. CX represents the CNOT gate [48]. These instructions are implemented using low-level hardware operations. For instance, the CX operator is implemented in hardware using a sequence consisting of cross-resonance gates and single-qubit rotation gates [47, 49, 50].

The *poughkeepsie* QPU is accessed remotely using a client-server interface. We employ the Qiskit programming language to specify the input circuit and test circuits for the GHZ-state preparation application [51]. These Pythonic programs are transpiled to the specifications and constraints of the backend, including ISA, connectivity layout, and register size. Additional inputs to the transpiler may include optimization protocols for minimizing circuit operations or noise levels. The transpiled programs are executed remotely on the *poughkeepsie* device, which returns the corresponding measurements along with job metadata.

We characterize measurement of all register elements in *poughkeepsie* and analyze the results using the SRO and ARO models. The results for direct estimation of the ARO model parameter p_0 and p_1 are shown in Fig. 4. The results for the SRO model correspond with $p_{sro} = p_0$. From these results, we observe a large spatial variability in readout error as well as asymmetry per register element. The readout of state $|1\rangle$ is almost always more error-prone than readout of state $|0\rangle$.

The results of estimating the parameter p_x for the depolarizing noise model of each X -gate are shown in Fig. 5. From these results, we see spatial variability in the recovered error parameter. We observe one case of a negative error rate for qubit 17 recovered from direct estimation using Eqs. 4 and 5. This is likely attributable either to inconsistencies in the error behavior for the test circuits such that the model cannot estimate a feasible parameter based on the results, or to errors for this register that are not well described by a depolarizing channel such that a different model may yield a better solution. All other error rates are relatively small and therefore we have not investigated model refinement for this case because of the negligi-

ble contribution to the noise.

We next characterize the Hadamard gate. We characterize error rates using test circuits generated from long sequences of Hadamards acting on a single element. We observe small error rates which correspond on average to 0.1% error per gate. We attempted to model the Hadamard noise using both a depolarizing channel and a unitary rotation, but neither model led to a better TVD than using a noiseless model for the gate. We concluded that error rates associated with the Hadamard operation are so small as to be negligible because the Hadamard noise was 100 times smaller than the next leading gate error.

We next characterize the Bell-state preparation circuits for each pair of possible interactions shown in Fig. 1. We use least-squares error estimation to find the value of p_{CNOT} that best fits the results while accounting for readout error as in Eq. (8). This approach yields more consistent results than solving each equation in the system explicitly and using a selection process to determine the final p_{CNOT} value from among these solutions which are often highly varied. The estimated parameter values are shown in Fig. 6.

We test the accuracy of the noisy subcircuit models with estimated parameters from experimental characterization. For these tests, we use explicit numerical simulation of the quantum state prepared by each noisy subcircuit model. We estimate the measurement outcomes for these modeled circuits using the simulated quantum state, and we compare these simulated observables with the corresponding experimental observations from the *poughkeepsie* device. The accuracy of the noisy subcircuit model is quantified using the total variation distance (TVD) defined in Eq. (1).

Our simulations of the quantum state use a numerical simulator bundled into the Qiskit software framework. The Aer software simulates both noiseless and noisy quantum circuits using the same Qiskit programs sent to the *poughkeepsie* device as input. We constrain the simulator to a statevector simulation method. Within Aer, we input the noise models using the error rates and noise operators of depolarizing and readout channels as defined in Sec. 3. Aer models gate noise using error functions parameterized

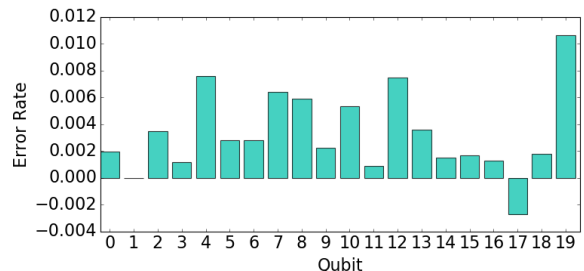


Figure 5: Depolarizing error rates associated with X gate application for each qubit of *poughkeepsie*. Average p_x value is 0.0033 with standard deviation 0.00303.

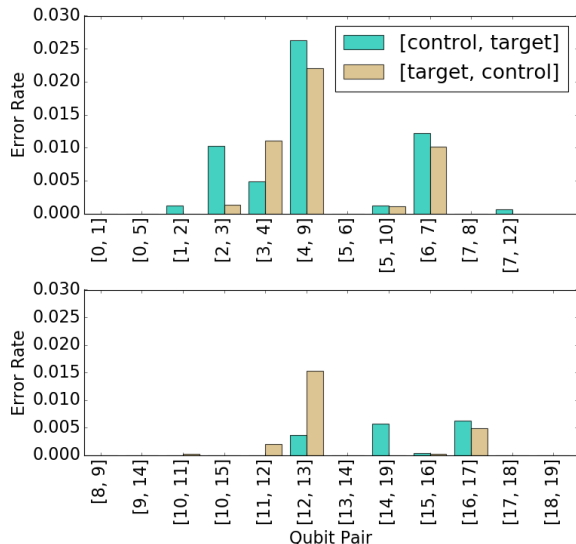


Figure 6: Error rates for CNOT gates under the depolarizing channel for each coupled qubit pair of *poughkeepsie*. These values are fitted to include the ARO channel noise with rates shown in Fig. 4.

by these error rates which create noisy descriptions of gates for simulation. When a noisy simulation is run, these functions sample errors and inject them as operations within the circuit. We tailor the simulations to match the developed noisy subcircuit models. Each test case acquired N_s samples in order to mimic the finite statistics from experimental characterization.

In addition, Aer provides a built-in noise model for the unitary gates and measurements that uses parameters derived from an RB protocol that is executed periodically as part of the IBM calibration and maintenance. We also execute simulations using this noise model using the parameters from RB available at the time of our data collection which are reported on the public repository [37]. These parameters are used as input to Aer as depolarizing channels associated with gate operations and a symmetric bit flip channel associated with readout [52].

A comparison of accuracy for different noisy subcircuit models is shown in Fig. 7 for simulating the Bell state circuit on qubits 0 and 1 on the *poughkeepsie* device. We calculate the TVD between experiment and simulation using seven different noise cases. We consider symmetric readout only (SRO), asymmetric readout only (ARO), CNOT depolarizing error only (DP), symmetric readout with CNOT error (SRO+DP), and asymmetric readout with CNOT error (ARO+DP). The error rate parameters are fit to the composite noise model, e.g. the depolarizing parameter in the SRO+DP case is not the same as in the ARO+DP case. We also simulate a noiseless Bell state and a Bell state using Aer’s built-in noisy device simulator for context and comparison. These results show that the noisy circuit model yielding the smallest TVD is composed from the asymmetric readout chan-

nel with a CNOT depolarizing channel (ARO+DP).

5 Performance Testing Results

We now present the performance of the selected composite model on n -qubit GHZ preparation circuits. Using the estimated ARO and CNOT error rates, we demonstrate iterations of this composite noise model which represent varying model complexity and experimental efficiency to achieve a particular accuracy. These iterations are shown in Fig. 8. The 2-qubit average case represents the performance of a noise model with only three parameters $p_0, p_1, p_{\text{CNOT}}$ —which are taken as the average of the error rates for only qubits 0 and 1. This represents a case of characterization using the fewest quantum resources, requiring only 7 experiments. We also consider a case which uses these same three parameters averaged over the entire register which retains low model complexity of only three noise parameters but requires the full suite of experiments. Our most detailed model accounts for spatial variations in the error parameters and uses individualized readout error rates for each qubit and CNOT error rates for each coupling. As with the Bell state example in Fig. 7, we show the noiseless case as well as noisy simulation using the built-in Aer noise model for the sake of context and comparison. Finally, we also show the sum of the minimum TVD achieved for noisy simulation of the Bell state across each qubit pair for which a CNOT was applied in the GHZ preparation circuit.

Figure 8 demonstrates a significant improvement in model accuracy for GHZ state preparation using our composite noisy circuit model. The improvement is a 3-fold decrease in TVD as compared to the noiseless simulation. Our fully spatial model always performs better than the intrinsic Aer model based on calibration data, while coarse-grained models, such as the average two-qubit model appear to be comparable to those derived from randomized benchmarking results. We also examine the scaling in the error with respect to the area of the circuit. We normalize the computed TVD by the number of CNOT gates in each GHZ preparation circuit, and we find that the per-qubit model accuracy is nearly constant across all

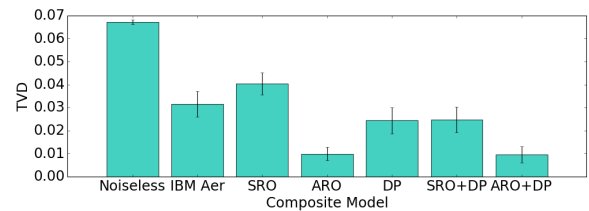


Figure 7: Comparison of possible choices for composite model. The best performance is achieved in the ARO+DP case. Error bars represent the distribution of TVD values across 100 sets of 8,192 samples per simulation case.

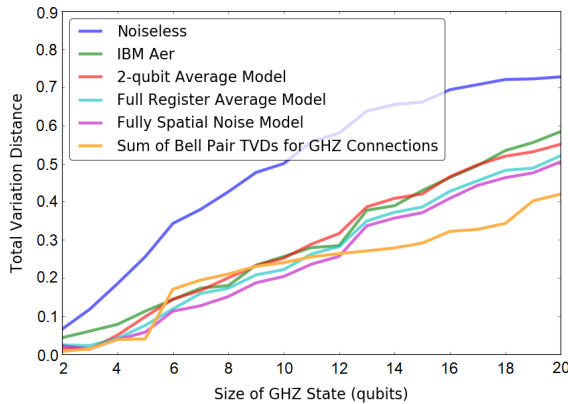


Figure 8: Performance of selected noise model on n -qubit GHZ states. The best performance is achieved with the fully spatial noise model.

GHZ circuit instances, as shown in Fig. 9. This trend would also hold when TVD is scaled by qubit count, since qubit count and CNOT count are strongly linked in the GHZ example. Since the TVD increases at a rate commensurate with CNOT count or qubit count, this may indicate that higher levels of entanglement or larger Hilbert spaces impact the predictability of noise in the device.

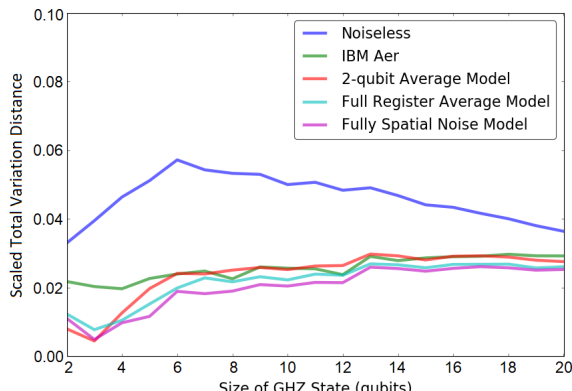


Figure 9: Scaled performance of selected noise model on n -qubit GHZ states, where TVD is divided by the number of CNOT gates in each circuit.

6 Bernstein-Vazirani Application

We next test the performance of this noisy circuit model on a different application to evaluate its ability to capture fundamental characteristics of the device. We test the performance by modeling several quantum circuit instances of the Bernstein-Vazirani algorithm. This algorithm considers a black box function that is encoded by a secret binary string which the Bernstein-Vazirani algorithm finds in one query [53]. Figure 10 shows an example of our circuit implementation of this algorithm using a three-bit string. We use a phase oracle qubit as the black box function

encoded with the secret string. Upon measurement of the non-oracle qubits we obtain the secret binary string. We select the Bernstein-Vazirani algorithm because it is implemented using the same gate set we have characterized for the GHZ example, so we do not require additional characterization circuits.

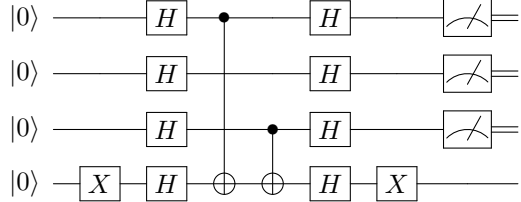


Figure 10: Circuit implementation of the Bernstein-Vazirani algorithm. The bottom qubit of the register is the oracle; the top three yield the secret string, here given as 101 as example. Other secret strings are produced by changing the CNOT gate sequence such that control qubits correspond to output bits of 1.

Given the connectivity constraints of the *pough-keepsie* device, the maximum bit string we can test without introducing SWAP operations is of length three. We choose qubits 6, 8, and 12 with oracle qubit 7 because this set has among the lowest error parameters. We execute the Bernstein-Vazirani algorithm for every possible encoding of the three-bit secret string and record the accuracy as the frequency that the encoded string was observed. We include collection of these measurements during the same job used to characterize the device.

Figure 11 plots the simulated accuracy of the circuit outcome using the fully spatial noise model alongside the experimental accuracy. Our model captures the decrease in experimental observed accuracy across the various binary strings. The loss in accuracy scales with the number of 1 bits in the secret string for both the experiment and simulation. However, the accuracy predicted by simulation is consistently higher than the accuracy observed experimentally, indicating a state-dependent noise source remains missing from this model.

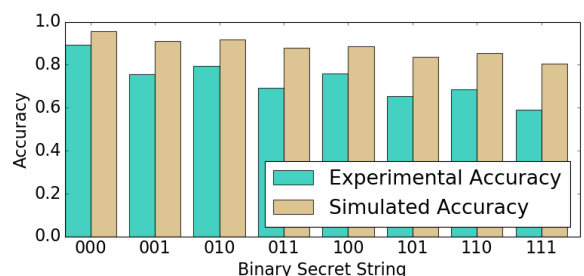


Figure 11: Performance of Bernstein-Vazirani algorithm evaluated as the measured frequency of the prepared secret string. Simulation is subject to noise defined by the fully spatial model.

7 Conclusion

We have presented an approach to noisy quantum circuit modeling based on experimental characterization. Our approach relies on composing subcircuit models to satisfy a desired accuracy threshold, model complexity, and experimental efficiency, which we implement using the total variation distance. We have tested our ideas using the IBM *poughkeepsie* device, which enables evaluation of our characterization methods as well as the comparison of predicted performance for GHZ state preparation and an instance of the Bernstein-Vazirani algorithm. The initial example focused on GHZ-state preparation examined model fidelity with respect to both width and depth of an input circuit. Models for the readout and CNOT subcircuits accounted for a majority of the model error. Our analysis of a second test circuit using instances of the Bernstein-Vazirani algorithm reveals additional sources of errors not captured in the original GHZ circuit characterization. Because both tests depend on the same gates for state preparation, the appearance of new errors suggests a possible state-dependent noise model that warrants further investigation. While our demonstrations have focused on specific devices and input circuits, the methodology provides a robust and flexible framework by which to generate noisy quantum circuit models on any device.

A significant feature of this approach to noise model decomposition is to iteratively adjust the models until sufficient accuracy is obtained. Improvements in accuracy may be obtained by changing characterization circuits or parameter estimation. The Bell state and GHZ state preparation examples demonstrate how this model adjustment may be performed by varying the experimental efficiency and the input to the model to change the accuracy of the final composite model. Our demonstrations have focused on the depolarizing channel for gate modeling, but circuit characterization can be directly extended to account for new noise models, components, applications, and algorithms. For example, in both the GHZ and Bernstein-Vazirani results, we observe an increase in TVD that scales with the number of CNOT gates applied in the circuit. A more sophisticated CNOT noise model may improve accuracy of the final noise model. Additionally, this methodology assumes separability in composition-decomposition. If this assumption is not true, the noise behavior for the selected subcircuits may not be the same as the composite circuits, meaning there may be an upper limit to the achievable accuracy of noise modeling using subcircuit testing. Further model refinement and testing would be necessary to demonstrate this non-separability.

Our original motivation was to address the growing challenge of characterizing NISQ applications, for which efficient and scalable methods are necessary. We have shown how to construct a set of test circuits

that scales with the area of the input circuit C and the underlying decomposition strategy. In the GHZ state preparation example, the number of total experiments needed for full spatial characterization scales with the size of the register q and the number of couplings c according to $N_s(2q + 2c + 1)$. This resource requirement enables characterization to be run alongside the state preparation circuit when the job is sent to the QPU. This efficiency should help ensure noise characterization is performed within the same processor context as the sought-after circuit. We anticipate such real-time characterizations to be valuable for dynamic compiling and tuning of quantum programs [35, 54, 55].

Our approach to characterization has relied on model selection using minimization of the total variation distance (TVD) between noisy simulation and experimental results. This demonstration used a small set of the possible models for characterizing the observed QPU behavior, and expanding the set of potential models is possible for future work. There is a necessary balance, however, between the sophistication of the model and the utility for characterizing QPU behavior. While fine-grain quantum physical models are capable of capturing a more detailed picture of the dynamics present on small scales, the dawning of the NISQ era requires the addition of new techniques to our toolbox that have a higher-level and larger-scale approach. For scalable numerical analysis of quantum computational methods, it is essential that we develop coarse-grained, top-down approaches to capture the core behavior of QPUs.

Acknowledgements

This research is supported by the Department of Energy Office of Science Early Career Research Program and used resources of the Oak Ridge Leadership Computing Facility, which is a DOE Office of Science User Facility supported under Contract DE-AC05-00OR22725. This manuscript has been authored by UT-Battelle, LLC under Contract No. DE-AC05-00OR22725 with the U.S. Department of Energy. The United States Government retains and the publisher, by accepting the article for publication, acknowledges that the United States Government retains a non-exclusive, paid-up, irrevocable, world-wide license to publish or reproduce the published form of this manuscript, or allow others to do so, for United States Government purposes. The Department of Energy will provide public access to these results of federally sponsored research in accordance with the DOE Public Access Plan. (<http://energy.gov/downloads/doe-public-access-plan>).

References

[1] Krysta M. Svore and Matthias Troyer. “The quantum future of computation”. In: *Computer* 49.9 (2016), pp. 21–30. DOI: [10.1109/MC.2016.293](https://doi.org/10.1109/MC.2016.293).

[2] Keith A. Britt and Travis S. Humble. “Instruction Set Architectures for Quantum Processing Units”. In: *High Performance Computing*. Ed. by Julian M. Kunkel et al. Cham: Springer International Publishing, 2017, pp. 98–105. ISBN: 978-3-319-67630-2. DOI: [10.1007/978-3-319-67630-2_8](https://doi.org/10.1007/978-3-319-67630-2_8).

[3] Alexander J. McCaskey et al. “A language and hardware independent approach to quantum-classical computing”. In: *SoftwareX* 7 (2018), pp. 245–254. DOI: [10.1016/j.softx.2018.07.007](https://doi.org/10.1016/j.softx.2018.07.007).

[4] Leon Riesebos et al. “Quantum Accelerated Computer Architectures”. In: *2019 IEEE International Symposium on Circuits and Systems (ISCAS)*. IEEE. 2019, pp. 1–4. DOI: [10.1109/ISCAS.2019.8702488](https://doi.org/10.1109/ISCAS.2019.8702488).

[5] Jay M. Gambetta, Jerry M. Chow, and Matthias Steffen. “Building logical qubits in a superconducting quantum computing system”. In: *npj Quantum Information* 3.1 (2017), p. 2. ISSN: 2056-6387. DOI: [10.1038/s41534-016-0004-0](https://doi.org/10.1038/s41534-016-0004-0).

[6] Frank Arute et al. “Quantum supremacy using a programmable superconducting processor”. In: *Nature* 574.7779 (2019), pp. 505–510. ISSN: 1476-4687. DOI: [10.1038/s41586-019-1666-5](https://doi.org/10.1038/s41586-019-1666-5).

[7] Matthew Reagor et al. “Demonstration of universal parametric entangling gates on a multi-qubit lattice”. In: *Science Advances* 4.2 (2018). DOI: [10.1126/sciadv.aao3603](https://doi.org/10.1126/sciadv.aao3603). eprint: <https://advances.sciencemag.org/content/4/2/eaao3603.full.pdf>. URL: <https://advances.sciencemag.org/content/4/2/eaao3603>.

[8] Ming Gong et al. “Genuine 12-Qubit Entanglement on a Superconducting Quantum Processor”. In: *Phys. Rev. Lett.* 122 (11 Mar. 2019), p. 110501. DOI: [10.1103/PhysRevLett.122.110501](https://doi.org/10.1103/PhysRevLett.122.110501). URL: <https://link.aps.org/doi/10.1103/PhysRevLett.122.110501>.

[9] Caroline Figgatt et al. “Parallel entangling operations on a universal ion-trap quantum computer”. In: *Nature* 572.7769 (2019), pp. 368–372. ISSN: 1476-4687. DOI: [10.1038/s41586-019-1427-5](https://doi.org/10.1038/s41586-019-1427-5).

[10] Thomas Monz et al. “Realization of a scalable Shor algorithm”. In: *Science* 351.6277 (2016), pp. 1068–1070. ISSN: 0036-8075. DOI: [10.1126/science.aad9480](https://doi.org/10.1126/science.aad9480). eprint: <https://science.sciencemag.org/content/351/6277/1068.full.pdf>. URL: <https://science.sciencemag.org/content/351/6277/1068>.

[11] Martin A. Sepiol et al. “Probing Qubit Memory Errors at the Part-per-Million Level”. In: *Phys. Rev. Lett.* 123 (11 Sept. 2019), p. 110503. DOI: [10.1103/PhysRevLett.123.110503](https://doi.org/10.1103/PhysRevLett.123.110503). URL: <https://link.aps.org/doi/10.1103/PhysRevLett.123.110503>.

[12] David Kielpinski, Chris Monroe, and David J. Wineland. “Architecture for a large-scale ion-trap quantum computer”. In: *Nature* 417.6890 (2002), pp. 709–711. ISSN: 1476-4687. DOI: [10.1038/nature00784](https://doi.org/10.1038/nature00784). URL: <https://doi.org/10.1038/nature00784>.

[13] John Preskill. “Quantum Computing in the NISQ era and beyond”. In: *Quantum* 2 (Aug. 2018), p. 79. ISSN: 2521-327X. DOI: [10.22331/q-2018-08-06-79](https://doi.org/10.22331/q-2018-08-06-79).

[14] Norbert M. Linke et al. “Experimental comparison of two quantum computing architectures”. In: *Proceedings of the National Academy of Sciences* 114.13 (2017), pp. 3305–3310. DOI: [10.1073/pnas.1618020114](https://doi.org/10.1073/pnas.1618020114).

[15] Abhinav Kandala et al. “Hardware-efficient variational quantum eigensolver for small molecules and quantum magnets”. In: *Nature* 549.7671 (2017), p. 242. DOI: [10.1038/nature23879](https://doi.org/10.1038/nature23879).

[16] Eugene F. Dumitrescu et al. “Cloud Quantum Computing of an Atomic Nucleus”. In: *Physical Review Letters* 120.21 (2018), p. 210501. DOI: [10.1103/PhysRevLett.120.210501](https://doi.org/10.1103/PhysRevLett.120.210501).

[17] Natalie Klco et al. “Quantum-classical computation of Schwinger model dynamics using quantum computers”. In: *Physical Review A* 98.3 (2018), p. 032331. DOI: [10.1103/PhysRevA.98.032331](https://doi.org/10.1103/PhysRevA.98.032331).

[18] Alexander J. McCaskey et al. “Quantum chemistry as a benchmark for near-term quantum computers”. In: *npj Quantum Information* 5.1 (2019), pp. 1–8. DOI: [10.1038/s41534-019-0209-0](https://doi.org/10.1038/s41534-019-0209-0).

[19] Andrzej Veitia et al. “Macroscopic instructions vs microscopic operations in quantum circuits”. In: *Physics Letters A* (2019), p. 126131. ISSN: 0375-9601. DOI: <https://doi.org/10.1016/j.physleta.2019.126131>. URL: <http://www.sciencedirect.com/science/article/pii/S0375960119310497>.

[20] Kenneth Rudinger et al. “Probing Context-Dependent Errors in Quantum Processors”. In: *Physical Review X* 9.2 (June 2019). ISSN: 2160-3308. DOI: [10.1103/physrevx.9.021045](https://doi.org/10.1103/physrevx.9.021045). URL: <http://dx.doi.org/10.1103/PhysRevX.9.021045>.

[21] Dietrich Leibfried et al. “Experimental Determination of the Motional Quantum State of a Trapped Atom”. In: *Phys. Rev. Lett.* 77 (21 Nov. 1996), pp. 4281–4285. DOI: [10.1103/PhysRevLett.77.4281](https://doi.org/10.1103/PhysRevLett.77.4281). URL: <https://link.aps.org/doi/10.1103/PhysRevLett.77.4281>.

[22] J.F. Poyatos, J. Ignacio Cirac, and Peter Zoller. “Complete characterization of a quantum process: the two-bit quantum gate”. In: *Physical Review Letters* 78.2 (1997), p. 390. DOI: [10.1103/PhysRevLett.78.390](https://doi.org/10.1103/PhysRevLett.78.390).

[23] Isaac L. Chuang and Michael A. Nielsen. “Prescription for experimental determination of the dynamics of a quantum black box”. In: *Journal of Modern Optics* 44.11-12 (Nov. 1997), pp. 2455–2467. ISSN: 1362-3044. DOI: [10.1080/09500349708231894](https://doi.org/10.1080/09500349708231894).

[24] Robin Blume-Kohout et al. *Robust, self-consistent, closed-form tomography of quantum logic gates on a trapped ion qubit*. 2013. arXiv: [1310.4492 \[quant-ph\]](https://arxiv.org/abs/1310.4492).

[25] Emanuel Knill et al. “Randomized benchmarking of quantum gates”. In: *Physical Review A* 77.1 (Jan. 2008), p. 012307. ISSN: 1094-1622. DOI: [10.1103/physreva.77.012307](https://doi.org/10.1103/physreva.77.012307). URL: <http://dx.doi.org/10.1103/PhysRevA.77.012307>.

[26] Easwar Magesan, Jay M. Gambetta, and Joseph Emerson. “Scalable and Robust Randomized Benchmarking of Quantum Processes”. In: *Phys. Rev. Lett.* 106 (18 May 2011), p. 180504. DOI: [10.1103/PhysRevLett.106.180504](https://doi.org/10.1103/PhysRevLett.106.180504). URL: <https://link.aps.org/doi/10.1103/PhysRevLett.106.180504>.

[27] Jonas Helsen et al. “Multiqubit randomized benchmarking using few samples”. In: *Phys. Rev. A* 100 (3 Sept. 2019), p. 032304. DOI: [10.1103/PhysRevA.100.032304](https://doi.org/10.1103/PhysRevA.100.032304). URL: <https://link.aps.org/doi/10.1103/PhysRevA.100.032304>.

[28] Mohammad J. Dousti and Massoud Pedram. “Minimizing the latency of quantum circuits during mapping to the ion-trap circuit fabric”. In: *2012 Design, Automation & Test in Europe Conference & Exhibition (DATE)* (Mar. 2012). DOI: [10.1109/date.2012.6176612](https://doi.org/10.1109/date.2012.6176612). URL: <http://dx.doi.org/10.1109/DAT.2012.6176612>.

[29] Frederic T. Chong, Diana Franklin, and Margaret Martonosi. “Programming languages and compiler design for realistic quantum hardware”. In: *Nature* 549.7671 (2017), p. 180. DOI: [10.1038/nature23459](https://doi.org/10.1038/nature23459).

[30] Yunong Shi et al. “Optimized Compilation of Aggregated Instructions for Realistic Quantum Computers”. In: *Proceedings of the Twenty-Fourth International Conference on Architectural Support for Programming Languages and Operating Systems - ASPLOS ’19* (2019). DOI: [10.1145/3297858.3304018](https://doi.org/10.1145/3297858.3304018). URL: <http://dx.doi.org/10.1145/3297858.3304018>.

[31] Andrew W. Cross et al. “Validating quantum computers using randomized model circuits”. In: *Phys. Rev. A* 100 (3 Sept. 2019), p. 032328. DOI: [10.1103/PhysRevA.100.032328](https://doi.org/10.1103/PhysRevA.100.032328). URL: <https://link.aps.org/doi/10.1103/PhysRevA.100.032328>.

[32] Robin Harper, Steven T. Flammia, and Joel J. Wallman. *Efficient learning of quantum noise*. 2019. arXiv: [1907.13022 \[quant-ph\]](https://arxiv.org/abs/1907.13022).

[33] Filip B. Maciejewski, Zoltán Zimborás, and Michał Oszmaniec. *Mitigation of readout noise in near-term quantum devices by classical post-processing based on detector tomography*. 2019. arXiv: [1907.08518 \[quant-ph\]](https://arxiv.org/abs/1907.08518).

[34] Swamit S. Tannu and Moinuddin K. Qureshi. “Not All Qubits Are Created Equal”. In: *Proceedings of the Twenty-Fourth International Conference on Architectural Support for Programming Languages and Operating Systems - ASPLOS ’19* (2019). DOI: [10.1145/3297858.3304007](https://doi.org/10.1145/3297858.3304007). URL: <http://dx.doi.org/10.1145/3297858.3304007>.

[35] Prakash Murali et al. “Noise-Adaptive Compiler Mappings for Noisy Intermediate-Scale Quantum Computers”. In: *Proceedings of the Twenty-Fourth International Conference on Architectural Support for Programming Languages and Operating Systems*. ASPLOS ’19. Providence, RI, USA: ACM, 2019, pp. 1015–1029. ISBN: 978-1-4503-6240-5. DOI: [10.1145/3297858.3304075](https://doi.org/10.1145/3297858.3304075). URL: <https://doi.acm.org/10.1145/3297858.3304075>.

[36] Angelo Bassi and Dirk-André Deckert. “Noise gates for decoherent quantum circuits”. In: *Physical Review A* 77.3 (Mar. 2008). ISSN: 1094-1622. DOI: [10.1103/physreva.77.032323](https://doi.org/10.1103/physreva.77.032323). URL: <http://dx.doi.org/10.1103/PhysRevA.77.032323>.

[37] Megan N. Lilly and Travis S. Humble. *Quantum Noise Modeling*. <https://code.ornl.gov/qci/characterization>. 2019.

[38] Jerry M. Chow et al. “Simple All-Microwave Entangling Gate for Fixed-Frequency Superconducting Qubits”. In: *Physical Review Letters* 107.8 (Aug. 2011). ISSN: 1079-7114. DOI: 10.1103/physrevlett.107.080502. URL: <http://dx.doi.org/10.1103/PhysRevLett.107.080502>.

[39] Sarah Sheldon et al. “Procedure for systematically tuning up cross-talk in the cross-resonance gate”. In: *Phys. Rev. A* 93 (6 June 2016), p. 060302. DOI: 10.1103/PhysRevA.93.060302. URL: <https://link.aps.org/doi/10.1103/PhysRevA.93.060302>.

[40] Diogo Cruz et al. “Efficient Quantum Algorithms for GHZ and W States, and Implementation on the IBM Quantum Computer”. In: *Advanced Quantum Technologies* 2.5-6 (2019), p. 1900015. DOI: 10.1002/qute.201900015. eprint: <https://onlinelibrary.wiley.com/doi/pdf/10.1002/qute.201900015>.

[41] Ken X. Wei et al. *Verifying Multipartite Entangled GHZ States via Multiple Quantum Coherences*. 2019. arXiv: 1905.05720 [quant-ph].

[42] Michael A. Nielsen and Isaac L. Chuang. *Quantum Computation and Quantum Information: 10th Anniversary Edition*. Cambridge University Press, 2010. DOI: 10.1017/CBO9780511976667.

[43] Easwar Magesan et al. “Machine Learning for Discriminating Quantum Measurement Trajectories and Improving Readout”. In: *Phys. Rev. Lett.* 114 (20 May 2015), p. 200501. DOI: 10.1103/PhysRevLett.114.200501. URL: <https://link.aps.org/doi/10.1103/PhysRevLett.114.200501>.

[44] Pauli Virtanen et al. “SciPy 1.0—Fundamental Algorithms for Scientific Computing in Python”. In: *arXiv preprint arXiv:1907.10121* (2019).

[45] Jens Koch et al. “Charge-insensitive qubit design derived from the Cooper pair box”. In: *Phys. Rev. A* 76 (4 Oct. 2007), p. 042319. DOI: 10.1103/PhysRevA.76.042319. URL: <https://link.aps.org/doi/10.1103/PhysRevA.76.042319>.

[46] Antonio D. Córcoles et al. “Demonstration of a quantum error detection code using a square lattice of four superconducting qubits”. In: *Nature communications* 6 (2015), p. 6979. DOI: 10.1038/ncomms7979.

[47] Andrew W. Cross et al. *Open Quantum Assembly Language*. 2017. arXiv: 1707.03429 [quant-ph].

[48] Abraham Asfaw et al. *Learn Quantum Computation Using Qiskit*. 2019. URL: <http://community.qiskit.org/textbook>.

[49] Maika Takita et al. “Experimental Demonstration of Fault-Tolerant State Preparation with Superconducting Qubits”. In: *Phys. Rev. Lett.* 119 (18 Oct. 2017), p. 180501. DOI: 10.1103/PhysRevLett.119.180501. URL: <https://link.aps.org/doi/10.1103/PhysRevLett.119.180501>.

[50] Chad Rigetti and Michel Devoret. “Fully microwave-tunable universal gates in superconducting qubits with linear couplings and fixed transition frequencies”. In: *Phys. Rev. B* 81 (13 Apr. 2010), p. 134507. DOI: 10.1103/PhysRevB.81.134507. URL: <https://link.aps.org/doi/10.1103/PhysRevB.81.134507>.

[51] IBM. *Qiskit Terra Documentation*. <https://qiskit.org/documentation/>. (19 December 2018).

[52] IBM Q. *Aer Release 0.2.3*. <http://github.com/Qiskit/qiskit-aer>. 2019.

[53] Ethan Bernstein and Umesh Vazirani. “Quantum Complexity Theory”. In: *SIAM Journal on Computing* 26.5 (1997), pp. 1411–1473. DOI: 10.1137/S0097539796300921. eprint: <https://doi.org/10.1137/S0097539796300921>.

[54] Swamit S. Tannu and Moinuddin K. Qureshi. “A case for variability-aware policies for nisq-era quantum computers”. In: *arXiv preprint arXiv:1805.10224* (2018).

[55] Ronald J. Sadlier and Travis S. Humble. “Near-optimal routing of noisy quantum states”. In: *Quantum Communications and Quantum Imaging XVII*. Ed. by Keith S. Deacon. Vol. 11134. International Society for Optics and Photonics. SPIE, 2019, pp. 28–39. DOI: 10.1117/12.2526670.